Synsint Research Group

Available online at www.synsint.com

Synthesis and Sintering

ISSN 2564-0186 (Print), **ISSN** 2564-0194 (Online)

Research article

Effects of die geometry and insulation on the energy and electrical parameters analyses of spark plasma sintered TiC ceramics

Milad Sakkaki [a,*], **Milad Foroutani** [b], **Peyman Zare** [c]

[a] *Department of Mechanical Engineering, Faculty of Manufacturing, University of Tabriz, Tabriz, Iran*
[b] *Department of Mechanical Engineering, University of Tarbiat Modares, Tehran, Iran*
[c] *Department of Electrical Engineering, University of Mohaghegh Ardabili, Ardabil, Iran*

ABSTRACT

This work conducts a numerical simulation to investigate the temperature and electric current distribution during the spark plasma sintering (SPS) process using the finite element method (FEM) carried out in COMSOL Multiphysics software. The main goal is to optimize the SPS process for titanium carbide (TiC) ceramics, with a particular focus on the effects of insulation and die geometry (height and thickness). For the TiC material, the ideal sintering temperature is set at 2000 °C. The study analyzes eight case studies, involving a base case, an insulating case, and six cases with various thicknesses and heights, to evaluate the effectiveness of the suggested optimization. The results show that using insulation on the die surface reduces heat transfer from the die surface significantly, which leads to a 63% decrease in input power consumption when compared to the basic scenario. Based on a correlation study between energy and electricity, increasing die thickness raises the cross-sectional area of the electric current, which raises the amount of electric power required to attain the 2000 °C sintering temperature. The results indicate the temperature distribution in the sample is more sensitive to changes in die height than to changes in die thickness.

KEYWORDS

Spark plasma sintering
UHTC
Electrical analysis
Energy optimization
Titanium carbide
Simulation

OPEN ACCESS

Abbreviation

Symbols	Description	Symbols	Description
FEM	Finite element method	UHP	Ultra-high pressure
UHTCs	Ultra-high temperature ceramics	TiC	Titanium carbide
SPS	Spark plasma sintering	ZrB_2	Zirconium diboride
TS	Two-step	h	Height
Hafnium diboride	HfB_2	t	Thickness
Aluminium oxide	Al_2O_3	RMS	Root-mean-square
Boron carbide	B_4C	ECR	Electric contact resistance
HP	High pressure		

* Corresponding author. *E-mail address:* sakkakimilad@student.uma.ac.ir, sakkakimilad@gmail.com (M. Sakkaki)
Received 15 August 2023; Received in revised form 23 January 2024; Accepted 24 January 2024.

https://doi.org/10.53063/synsint.2024.41172

Notation	Description
J	Current density vector
∇J	Gradient of the current density vector
σ	Electrical conductivity
E	Electric field
∇(σE)	Gradient of the product of σ and E
U	Gradient of electric potential
∇(-σ∇U)	Gradient of negative product of σ and U
ρ	Material density
CP	Specific heat capacity
∂T/∂r	Radial temperature gradients
∂T/∂z	Axial temperature gradients
q_i	Internal heat generation or absorption
r	Radial coordinate
z	Axial coordinate
i_r	Radial component of current density
i_z	Axial component of current density
u	Voltage waveform
t	Present time
T	Period time
K	Kelvin
P	Power
I	Current
V	Voltage
q_c	Dissipated heat flux by the water
h_c	Convection coefficient
T_s	Surface temperature
T_w	Water temperature
q_r	Radiation heat flux
ε	Material emissivity
σ_s	Stefan–Boltzmann constant
T_e	Emission surface temperature
T_a	Chamber walls temperature
MPa	Mega Pascal
mm	millimeters

1. Introduction

1.1. Background of research

Ultra-high-temperature ceramics, known as UHTCs, are advanced materials that have unique features, particularly when exposed to extreme temperatures [1, 2]. These materials are gradually attracting attention as durable candidates for a wide range of industrial applications that require resistance to harsh environments, high mechanical strength, and extreme temperatures [3–7]. UHTCs have become known for their remarkable thermal stability, exceptional mechanical properties, and compliance with a wide range of substances [8–14]. The manufacturing of UHTCs is almost a challenge due to their low self-diffusion caused by covalent bonding, weak sinterability, and high melting temperature [15–17]. It tends to be challenging to achieve a balance between improved sinterability and controlled grain growth.

Preserving fine-grain structures and optimizing the synthesis process are two of the main challenges associated with conventional powder metallurgy methods, such as hot pressing, in the manufacturing of metal [18, 19]. The SPS method simultaneously applies both external pressure and electric current to the material during the sintering process. Applying high pressure during the sintering process is one of the major advantages of using SPS. This eliminates porosity and voids, leading to a more effective synthesis process. External pressure is applied. Because it directly influences the mechanical and thermal properties of materials, accurate control of grain development is essential for numerous metallurgical applications. SPS offers this control and fine-grained microstructures—which are frequently necessary in a variety of technical applications—through a distinctive combination of rapid heating and brief holding times [20–27]. SPS has several advantages over conventional methods. In particular, rapid heating and short holding time reduce processing time. In addition, SPS operates at lower sintering temperatures, which helps with energy conservation and preserves the integrity of temperature-sensitive materials. In contrast to traditional powder metallurgy techniques, SPS presents a promising alternative that could enhance ceramic synthesis while effectively controlling grain size [28–32]. Compared to the conductive heat transport used in conventional sintering systems, using volumetric heating rates caused by the Joule effect enables a rapid increase in temperature. This phenomenon increases the mass transport mechanisms responsible for sintering processes, resulting in a higher consolidation rate and less grain coarsening. This restriction in grain coarsening improves the mechanical and physical properties of the final sintered parts, including enhanced mechanical strength and structural integrity [33–35].

Although the experimental method is utilized, the determination of the temperature distribution in spark plasma sintering can be accomplished by the utilization of finite element modeling, which is helpful. The process can be managed and optimized with the help of this strategy, which takes into consideration the interrelated phenomena that are involved.

1.2. Literature survey

Considering the preceding discourse, it is evident that a research initiative is currently underway to optimize the SPS process by implementing insulation and die geometry optimization. Research in this area is extensive and delves into several facets, including the simultaneous application of external pressure and electric parameters, a broad range of optimization procedures, design methodologies, and various configurations. Scholarly articles addressing the optimization of the SPS process have increased significantly in recent years. Therefore, to determine the research gaps in the studies, we will conduct a comprehensive review of them so that the present study may contribute to filling the research gaps.

Via the present research on Spark Plasma Sintering by Zhang et al. [36]. The thermal-electric-mechanical model is introduced by a detailed and comprehensive model prototype. The result showed that there was a radial temperature of 155 °C and an axial of 24 °C. Computer simulations obtained stress gradients, which were compared with theoretical ones (0.9699). Finally, to improve the efficiency of the device by considering the temperature, they suggested a reduced

diameter for the die. With the approach to temperature measurement in SPS, researchers can enhance the efficacy and reliability.

Nöthe et al. [37] conducted a finite element model and a customized setup for in-depth analyses of spark plasma sintering. A testing environment interacting with a finite element model was constructed that enabled thorough analysis. Being small, this setup generates aperture currents, an arbitrary waveform, pressure variations, and dilatometry readings at the same time. They also found temperature dependence from contact resistances and furnace configuration and unequal currents caused by uneven interfacial contacts between the foil and specimen. As well, they found the potential variance in currents due to imperfect contacts at graphite foil and specimen interfaces.

Semenov et al. [38] applied a numerical modeling method to investigate the early stages of sintering of a particle assembly under spark plasma sintering on a microscopic scale. The fully laminated thermo-electro-mechanical problem, which takes into account the grain boundaries and the transport at surfaces, is solved using the staggered method.

Ranjbarpour Niari et al. [39] use numerical simulations to study the spark plasma sintering process of HfB_2. Electrical conductivity is one of the main properties of HfB_2 that allows for the uniform distribution of the flow during sintering and gives it an advantage over other non-conductive ceramics. The combination of the Joule effect in thermal distribution proves HfB_2 to be exclusive, indicating chances for better and more moderated SPS approaches in materials science and process manufacturing, especially pertinent to industrial applications when targeting electrical conductivity.

Bagheri et al. [40] highlight the importance of numerical simulations in investigating and optimizing the SPS process for TiC samples. By solving governing equations for heat conduction and electric current distribution, the study successfully achieves the desired sintering temperature of 2000 °C. They reported a radial temperature gradient of 80 °C in the TiC sample. Although their reports indicate that the maximum temperature occurs at the die and punch interface, where the cross-section is minimum and current density is highest, as a result, heat generation via Joule heating phenomena is highest.

Sakkaki et al. [41], in a numerical simulation, investigated the temperature and electric current distribution via the FE method in the SPS process of the ZrB_2 and Al_2O_3 samples. They attempt to clarify the temperature and electric current distribution in conductive and non-conductive materials to gain a clear understanding of the heat transfer mechanism and temperature distribution in the sample. They reported different mechanisms of heating for the sintering process of ZrB_2 and Al_2O_3. Al_2O_3, as an electrical insulator, concentrates the electric current in the graphite die near the sample, whereas ZrB_2, as an electric conductor, promotes a more uniform distribution of current. The graphite die generates and conducts heat to the non-conductive sample. On the other hand, the sintering process of ZrB_2 involves both the Joule heating effect and thermal conduction from the die to the sample. They also reported that the temperature distribution in non-conductive materials is more uniform than in conductive materials.

1.3. Contributions of this paper

In response to the identified research gaps within the domain of SPS research, the presented context involves:

- Energy efficiency analysis: a strategy focused on energy consumption;
- correlation analysis;
- investigation of radiant heat transfer with a particular focus on the die surface.

1.4. Organization of the paper

This paper adheres to the following sections within a meticulously structured framework:

The methodology and solution method are presented in section 2. Sections 3 and 4 present the findings and discussions. An overview of the correlation study between electrical power and thermal losses is given in section 5. Lastly, section 6 presents the conclusions.

2. Methodology

2.1. Geometry

The geometry of the SPS system, which was used in the numerical simulation, is shown in Fig. 1. The device consists of spacers, graphite punches, and upper and lower electrodes. Water current cools both the lower and upper electrodes, which are made of Inconel. The presented numerical simulation attempts to evaluate the effect of die geometry on energy consumption in the SPS process, namely die thickness (t) and height (h).

2.2. Mathematical formulation of geometric relationships

Due to the Joule heating phenomenon, heat is produced during the spark plasma sintering process when an electric current passes through the material. For each point, the temperature distribution can be obtained by solving the Maxwell and electric charge conservation equations. In addition, the heat diffusion equation has to be solved to determine the temperature distribution. Furthermore, the need to link and concurrently solve these equations is emphasized due to the temperature-dependent properties involved. Eq. 1, which is based on Ref. [41], describes the Maxwell equation:

$$\nabla J = \nabla\left(\sigma E\right) = \nabla\left(-\sigma \nabla U\right) = 0 \tag{1}$$

where E, J, U, and σ are the electric field, the current density, the electric potential, and the electrical conductivity of the materials, respectively.

The energy equation in cylindrical coordinates is represented by Eq. 2.

$$\rho C_P \frac{\partial T}{\partial t} = \frac{1}{r}\frac{\partial}{\partial r}\left(rk_r \frac{\partial T}{\partial r}\right) + \frac{1}{z}\frac{\partial}{\partial z}\left(rk_z \frac{\partial T}{\partial z}\right) + q_i \tag{2}$$

k_r and k_z are the thermal conductivity in the r and z directions, respectively. C_p shows the heat capacity, T is the temperature and ρ is the density.

Eq. 2 describes the balance of thermal energy within a cylindrical region, accounting for conduction in both the radial and axial directions, along with any internal heat sources or sinks. The first term, $\rho C_p\ \partial T/\partial t$, signifies the rate of temperature change concerning time, where ρ is the density of the material and C_p is its specific heat capacity. The following two terms account for heat conduction in the radial (r) and axial (z) directions, incorporating the radial and axial temperature gradients ($\partial T/\partial r$ and $\partial T/\partial z$, respectively). These terms also consider variations in material properties, such as density and thermal conductivity, along with the respective coordinates. The final term, q_i represents any internal heat generation or absorption within the system, this term is defined as:

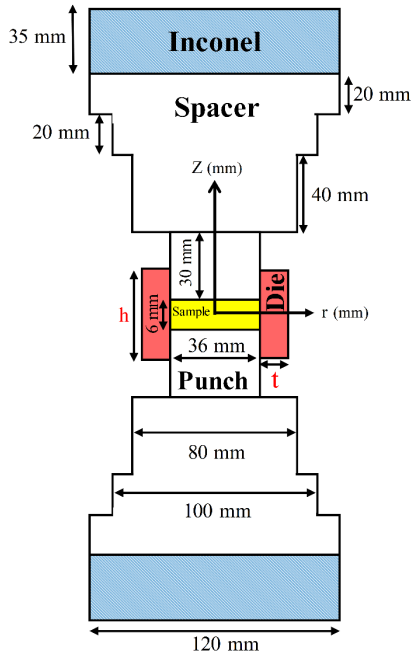

Fig. 1. A schematic representation of the SPS geometry.

$$q_i = J.E \quad (3)$$

where E is the electric field.

Hereafter, the expression for electric current in cylindrical coordinates is conventionally denoted as Eq. 4:

$$\frac{1}{r}\frac{\partial(ri_r)}{\partial r} + \frac{\partial i_z}{\partial z} = 0 \quad (4)$$

The parameters are as follows: "r" represents the radial coordinate, "z" is the axial coordinate, "i_r" is the radial component of current density, and "i_z" is the axial component of current density.

Setting the RMS values for voltage and current intensity is necessary for calculating power dissipation in heating tools. The passion of the electrical signal is measured by these RMS values, to demonstrate the amount of energy lost as heat. Determining these is essential for accurately calculating the heating tool's power dissipation. A certain equation must be used to calculate the RMS voltage value [43]. This process step is of extreme importance since it makes it possible to take into account the effective voltage and current values, which are vital for accurately determining the power used by heating equipment. Using RMS values provides a more accurate representation of power usage since it offers a metric that takes into account both the amplitude and time-varying properties of electricity.

Due to the lack of space, the additional fundamental relationships between energy and electrical parameters, such as voltage, electric current, and electric power, are not shown. However, a complete definition of these relationships can be found in [44–46]. Hence, the equation governing the determination of the RMS value of voltage is articulated as follows in Eq. 5:

$$U_{RMS} = \sqrt{\frac{1}{P}\int_{t-T}^{t} u^2(\tau)d\tau} \quad (5)$$

The integral term $\int_{t-T}^{t} u^2(\tau)d\tau$ calculates the square of the voltage waveform "u" over a time interval from "t - T" to "t," where "t" is the present time, and "T" is the period considered for calculating the RMS value. The division by "P" signifies that the voltage waveform's power is divided by the period "T". The RMS voltage is a measure that considers both amplitude and the waveform's temporal characteristics, facilitating accurate power calculations and equipment assessment.

2.3. Characteristics of materials

The electrical and thermal properties are closely related to the thermoelectric problems. The temperature range in the sintering process is large, so it is important to take the temperature dependence of the material properties into account. Table 1 lists the characteristics of the materials.

2.4. Parameters for boundaries and initial states

The governing equations necessitate corresponding boundaries and initial conditions for a comprehensive solution. The applying boundary conditions in this paper are presented in Fig. 2, where electrical insulation is implemented on the outer surfaces of the device (depicted by brick red and yellow lines in Fig. 2). When applying an electric potential, the upper surface is connected to the ground. In contrast, the lower surface is grounded (i.e., V = 0). As observed in Fig. 2, water flows over both the upper and lower surfaces, undergoing convective heat transfer, which is mathematically described by Newton's cooling law as Eq. 6:

$$q_c = h_c(T_s - T_w) \quad (6)$$

Table 1. The properties of different parts of the SPS system as functions of temperature (T in Kelvin).

Material	Heat capacity ($J.kg^{-1}.K^{-1}$)	Density ($kg.m^{-3}$)	Thermal conductivity ($W.m^{-1}.K^{-1}$)	Electrical resistivity (Ω.m)
Graphite [47]	$34.27+2.72\times10^{-4}\times T^2$	$1.9\times10^{-3}-1.414\times10^{-2}\times T$	$82.85-0.06\times2.56\times10^{-5}\times T^2$	$2.14\times10^{-5}-1.34\times10^{-8}\times T+4.42\times10^{-12}\times T^2$
Inconel	$344+0.25\times T$ [42]	8.43×10^{3} [53]	$0.0157\times T+10.09$ [53]	$9.82\times10^{-7}+1.6\times10^{-10}\times T$ [53]
TiC	$803+5.744\times10^{-2}T-5.427\times10^{-5}T^2-23.685\times10^{6}/T^2$ [56]	4930 [57]	$9.8\times10^{-3}T+23.994$ [58]	$1/(6\times10^{-10}T+4\times10^{-7})$ [58]

Remark: ($J.kg^{-1}.K^{-1}$): Joule per kelvin per kilogram; ($kg.m^{-3}$): kilogram per cubic meter; ($W.m^{-1}.K^{-1}$): watts per meter-kelvin; (Ωm): ohm-meter.

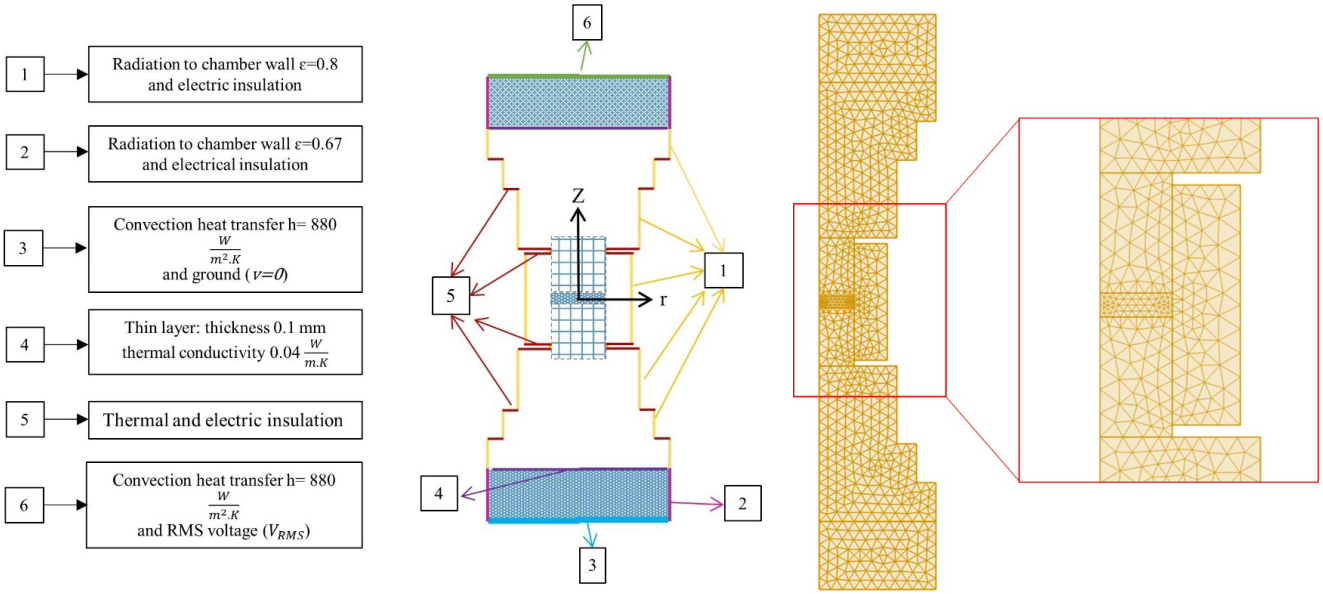

Fig. 2. Applied boundary conditions and mesh.

Adapted from Ref. [47], the convection coefficient for both upper and lower surfaces is considered to be h_c = 880 $W.m^{-2}.K^{-1}$ [48]. The sintering setup operates within a vacuum environment; therefore, heat losses from the side walls are exclusively considered radiation. The heat transfer through the radiation mechanism can be mathematically expressed as in Eq. 7:

$$q_r = \sigma_s.\varepsilon.\left(T_e^4 - T_a^4\right) \quad (7)$$

As per Refs. [48, 49], the material emissivity values are set at 0.8 [50] for graphite and 0.67 [51] for Inconel. It is proposed to apply a thermal contact layer with a thickness of 0.1 mm and a thermal conductivity of 0.04 $W.m^{-1}.K^{-1}$ [49] at the interface between Inconel and the spacer (see Fig. 2). It is noteworthy that Manière et al. [52] observed that when temperatures exceed 800 °C and pressures surpass 50 MPa, the ECR becomes negligible. Given that the working pressure in this study is approximately 100 MPa, the ECR is presumed to be zero. Furthermore, the sintering temperature is set at 2000 °C [53, 54].

3. Solution methodology

The finite element method is a powerful computational tool that is utilized to analyze and solve engineering problems. The model-governing equations are solved with the help of the finite element method, which is accomplished with the software COMSOL Multiphysics (version 6.14). Engineering problems can be analyzed and solved with the help of finite element modeling (FEM), which is a powerful computational technique [55]. In an accurate simulation, it is necessary to choose a suitable mesh size. Fig. 2 illustrates the mesh that was applied, which contains triangular elements. To conduct a more accurate analysis, the sample section takes into consideration a smaller mesh size. Ultimately, 1430 elements are chosen for this research project, which investigates a variety of mesh sizes to establish mesh independence.

4. Results and discussion

This research effort attempts to clarify how insulation and geometrical characteristics (thickness and height) affect the amount of energy used in the SPS process. In this paper, the variations in the TiC sample die's thickness and height are investigated, and the power required to reach the constant sintering temperature (2000 °C) is calculated. Optimizing the SPS process becomes related to a better understanding of the temperature distribution, the effect of die geometrical characteristics, and the use of insulation during the SPS process. These approaches give an accurate understanding of the modified die's energy usage as well as its electrical characteristics, including power, voltage, and current.

4.1. Validation analysis

The presented numerical simulation validation was verified by comparing temperature distributions in a computational area that was the same as Pavia et al. [53], the results of which are presented in Fig. 3. Referring to Fig. 3, there is a good agreement between Pavia et al. [53] investigation results. Thus, the proposed numerical method can be used to simulate the sintering process of a TiC sample.

4.2. Analysis of radial temperature distribution based on thickness and height of die

The radial temperature distribution in the sample along die thickness and height is illustrated in Figs. 4 and 5, respectively. In both cases, the temperature gradient from the sample center to the die surface exhibits a decreasing trend. As shown in Fig. 4, the changes in the temperature gradient from the center to the edge of the sample (r = 18) are similar. This is because the heat generated in the core of the sample is dissipated into the surroundings, resulting in a decreased temperature gradient from center to edge.

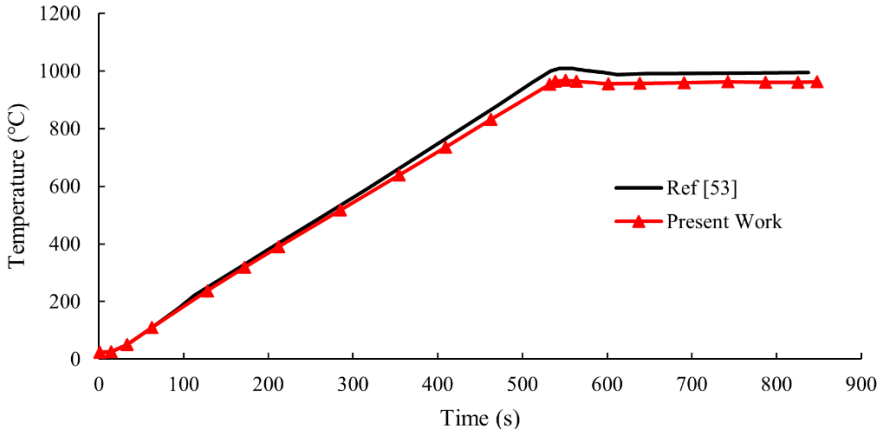

Fig. 3. Validation of the present work using the data provided by Pavia et al. [53].

In Fig. 5, the temperature pattern is similar to Fig. 4. According to Fig. 5, the die experiences a lower temperature difference with an increase in the height of the sample die. Also, in the sample, the slope of the temperature reduction decreases with the increase in the height of the die. The radial temperature distribution has a significant effect on the final sample microstructure. A sample with a smaller temperature difference tends to have more uniform mechanical and microstructural properties. Additionally, as depicted in Fig. 5, in contrast to die thickness variations, die height alterations induce modifications in the temperature distribution pattern. To achieve a uniform temperature distribution, it is necessary to choose either a die with a lower thickness or a die with a higher height [54]. Upon comparing both Fig. 4 and Fig. 5, it becomes evident that to achieve a more uniform temperature distribution, selecting a die with greater height and reduced thickness proves to be effective in the optimization process. Therefore, a die with a shorter height and reduced thickness is the preferred option for optimizing temperature distribution.

4.3. Temperature contours analysis

To find out the correlation between electric current lines and temperature distribution in all components, the temperature contour and electric current lines for the study cases were derived. To conduct a comparative study, all temperature distribution contours and electric current lines were projected symmetrically. In each figure, the right side of the symmetry axis corresponds to the electric current lines, while the left side corresponds to the temperature distribution contour.
In all cases, the interface between the punch and the spacer exhibits the maximum current density, as shown in Figs. 6–8. This occurrence is attributed to the reduced cross-sectional area of the current path from the spacer to the punch. Consequently, this phenomenon contributes to generating maximum temperatures in this area. The central region of the system consistently exhibits the highest temperature across all cases. A gradual decrease in the temperature gradient is obvious as it moves away from the center. All analyzed cases consistently identify this characteristic pattern of temperature distribution and electric current lines.

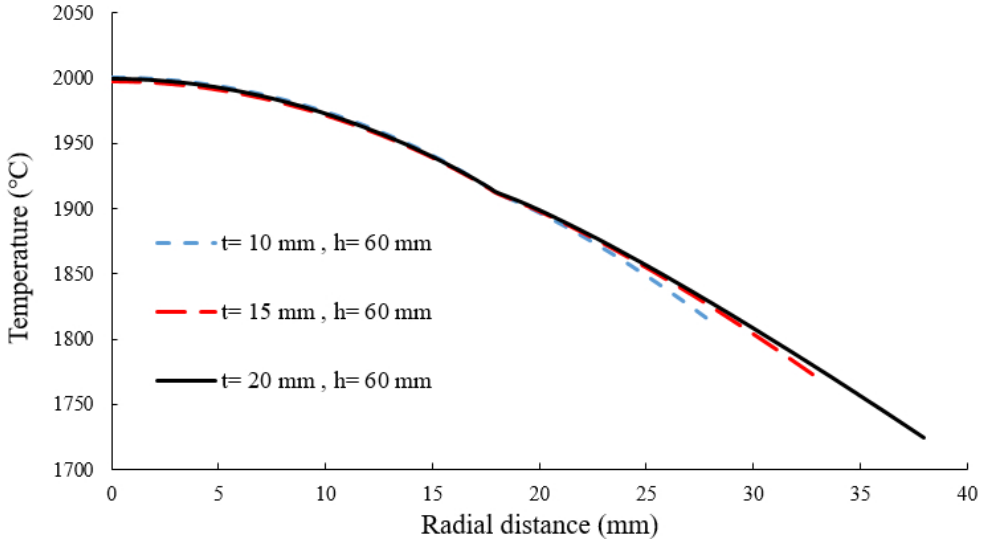

Fig. 4. The radial temperature distribution of the sintered sample at various thicknesses (constant height of die; h=60 mm).

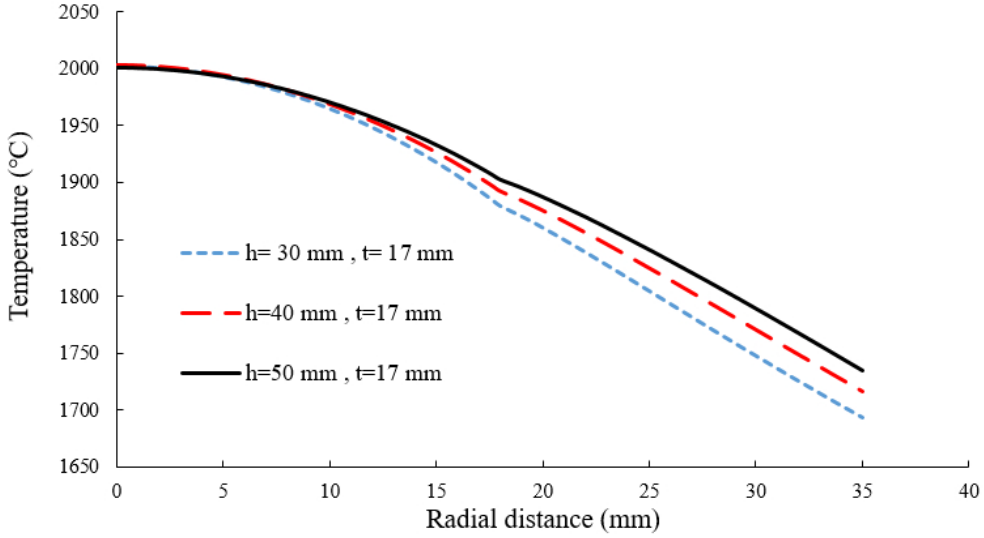

Fig. 5. The radial temperature distribution of the sintered sample at various heights (constant thickness of die; t=17 mm).

4.3.1. Effect of die insulation

Fig. 6 shows the electric current lines and temperature distribution contour of the base and insulated cases. In both the insulation case and the base case, the distribution pattern of electric current lines remains unchanged. The temperature distribution in the punch, sample, and die, however, indicates a good level of uniformity when compared to the base case because of the insulated case's surface insulation and a lack of heat losses from the die surface. In the base case, the temperature differential between the surface of the die and the center of the sample is 246 °C. This temperature differential, nevertheless, is only 0.3 °C in the insulated sample. In addition to reducing the amount of electrical power needed for the SPS process and reducing thermal energy losses, this decrease in temperature difference causes the sample's temperature to be more uniform, which improves the sample's mechanical and micromechanical characteristics.

4.3.2. Effect of die height

Fig. 7 shows the temperature distribution contour and electric current lines based on die height variation. According to Fig. 7,

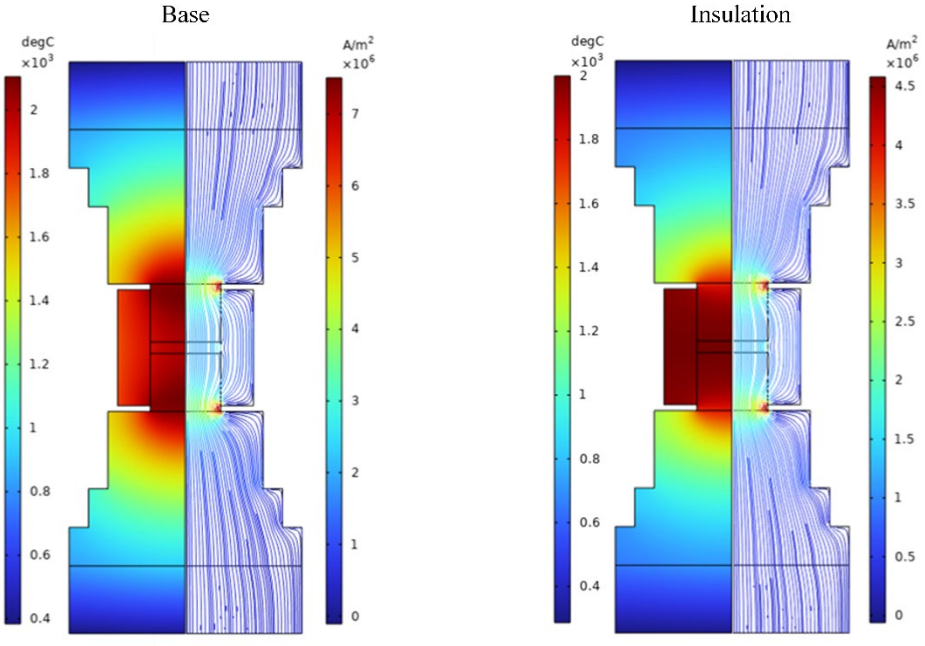

Fig. 6. Temperature distribution contours and electric current lines for the base and insulation cases.

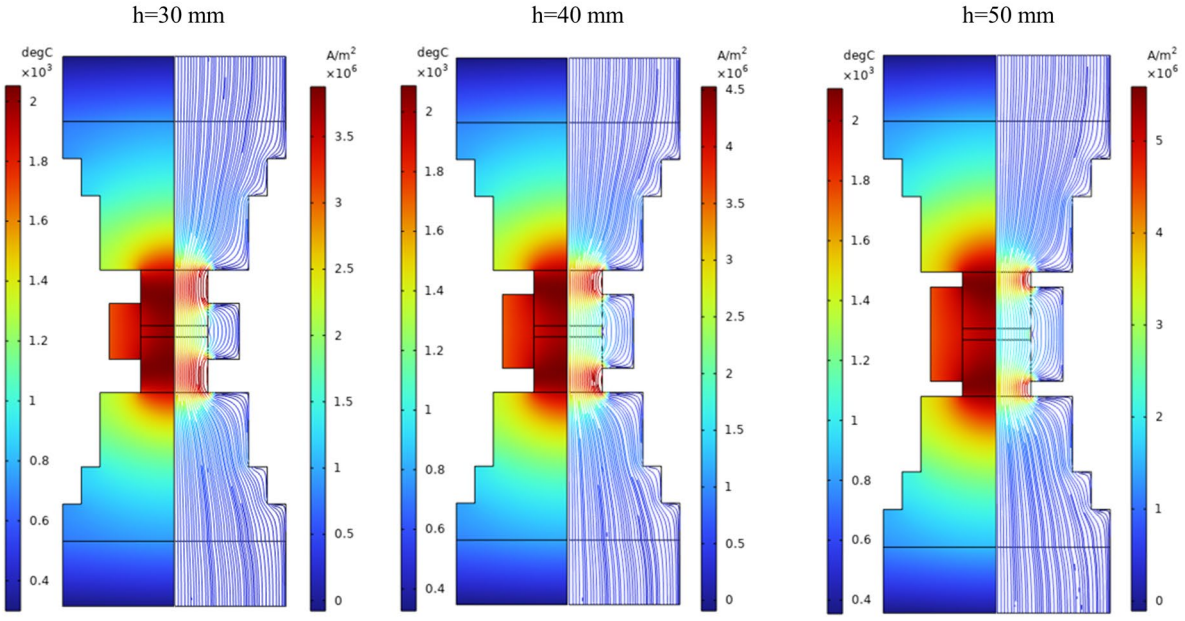

Fig. 7. Temperature distribution contours and electric current lines for the various die height.

the height of the die greatly affects the pattern of electric current line distribution. A shorter die height decreases the pass cross-sectional area of the electric current in the die, leading to a higher electric current in the sample. Increasing the die height increases the cross-sectional area of the passing electric current, therefore generating more heat. The die with a higher height shows a higher temperature than a die with a shorter height, as shown in Fig. 5. Further, the electrical current line density in the punch and sample is greater than in a die with a larger height; as a result, the punch temperature and heat generation around the sample increase. In a die with a shorter height, where heat generation is lower, the temperature difference between the sample and the die is higher. This leads to more heat transfer from the sample to the die via the conductive heat transfer mechanism, resulting in a more non-uniform temperature distribution in the sample. Hence, selecting the optimal die height minimizes sample heat loss and temperature differences.

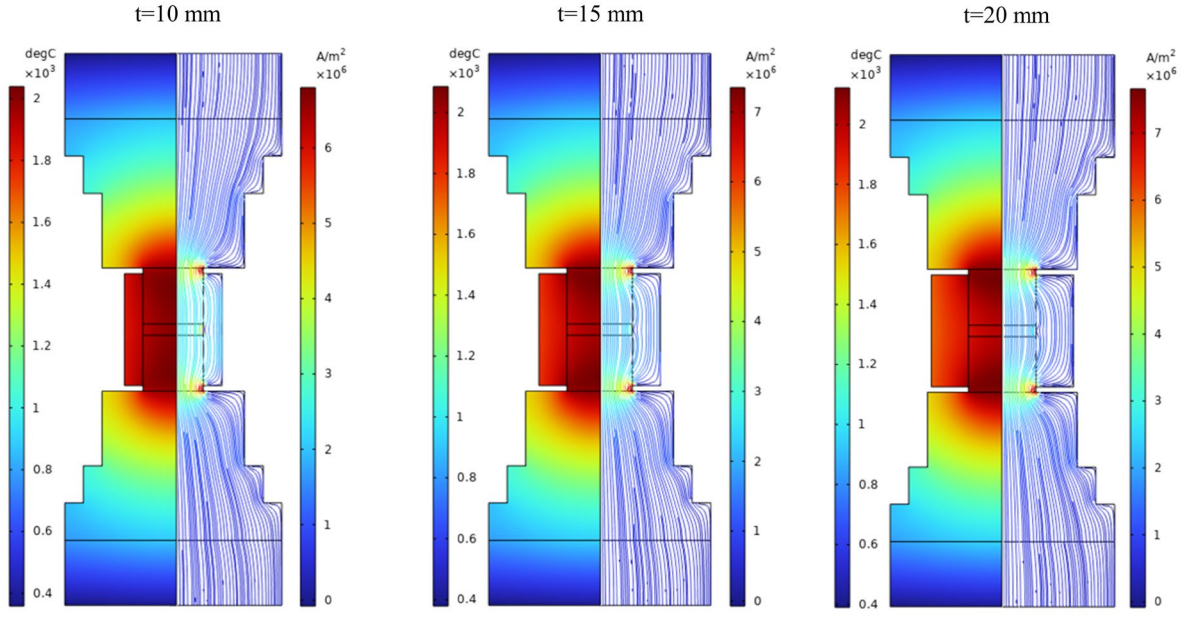

Fig. 8. Temperature distribution contours and electric current lines for the various die thickness.

Table 2. Electric current, voltage, and power consumption at different heights and thicknesses.

Case study	Profile		Voltage (V)	Current (A)	Power (kW)
	t (mm)	h (mm)			
(1) Base	17	60	5.07	5684.6	28.82
(2) Insulation	17	60	2.99	3498	10.45
3	17	30	4.27	3714.4	15.86
4	17	40	4.62	4288.5	19.81
5	17	50	4.89	4936	24.13
6	10	60	4.85	5207.3	25.25
7	15	60	5.01	5577.5	27.94
8	20	60	5.12	5791.5	29.65

Remark: V:volt; A: ampere; kW: kilo Watt.

4.3.3. Effect of die thickness

Fig. 8 delivers the temperature distribution contour and electric current lines based on the effect of die thickness. In all cases, the maximum current density and the maximum temperature variation are similar to the previous section that was discussed. Fig. 8 shows that an increase in die thickness results in a higher current density within the die due to the expanded cross-sectional area. Also, a die with an increased thickness shows a more uniform distribution of current lines than a thinner die. The higher current density in the thicker die also leads to elevated heat generation, resulting in increased heat losses and a non-uniform temperature distribution in the die. The lower current density in the sample within the thicker die reduces Joule heating compared to the thinner die. These observations highlight that employing a die with the optimal minimum thickness minimizes heat loss and reduces temperature differences in the die.

4.4. Correlation energy and electrical analysis

Table 2 shows the electrical and energy analysis results (current, voltage, and power consumption) at different thicknesses and heights. Considering that the sintering temperature (at the sample's center) has been maintained constant in the simulation in all cases, different electric power consumptions have been calculated to achieve this fixed temperature (2000 °C). This highlighted the importance of optimizing the geometrical parameters. Furthermore, the voltage, current, and power consumption in the base case are 5.07 V, 5684.6 A, and 28.82 kW, in that order. In the insulated case, these values fall to 2.99 V, 3498 A, and 10.45 kW, which represents a 63% reduction in electrical power consumption due to radiation heat transfer from the die surface. This indicates that preserving the system from radiation heat transfer reduces electrical power consumption, which lowers the energy required to power the system.

The insulated case exhibits considerably less electric power consumption than the other cases, according to the results. Fig. 9 compares the increase in power savings in the insulation mode to the other cases. The power reductions are 34%, 47%, 56%, 58%, 62%, and 64%, respectively, when comparing the insulated case 3 to case 8. This is because insulation reduces heat losses through radiation heat transfer.

The power consumption in terms of die thickness is shown in Fig. 10. The electric power consumption curve is depicted using three distinct thicknesses (t = 10 mm, t = 15 mm, and t = 20 mm) and a constant height (h = 60 mm). Results indicate that as die thickness increases, it also increases electric power consumption. These three thicknesses require, in order, 25.25, 27.94, and 29.65 kW of electric power.

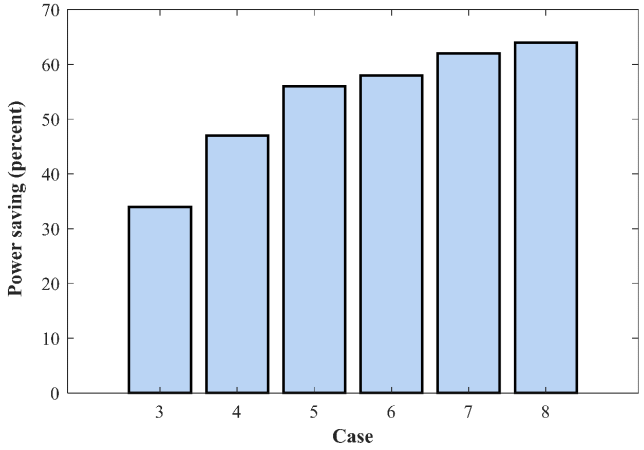

Fig. 9. Percentage of power saving in insulated mode compared to case studies 3 to 8.

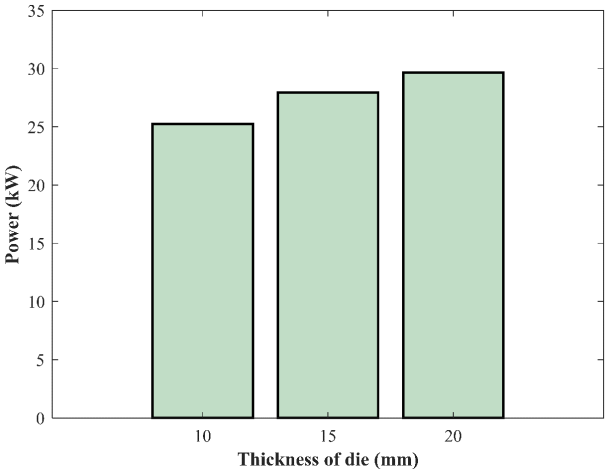

Fig. 10. Power consumption in the various thicknesses of the die (constant height of die; h=60 mm).

Fig. 11 shows electric power consumption based on the die different height at a constant thickness (t = 17 mm).

The electric power consumption for h = 30 mm, h = 40 mm, and h = 50 mm is 15.86, 19.81, and 24.13 kW, respectively. As is obvious, increasing die height led to a higher electric power consumption requirement.

Electric power and radiation flux are directly related to each other, so the level of electric power affects the radiant flux. An analysis delineating the changes in radiant heat flux has been provided using Figs. 12 and 13. Fig. 12 displays the radiated heat flux from the entire device's wall surface for various cases. The radiant heat flux is 21.46 kW in the base state and reduces to 5.51 kW in the insulation state. For cases 3 to 8, these values are 10.3, 13.6, 17.41, 18.44, 20.71, and 22.17 kW, respectively. Fig. 12 clearly shows that selecting larger height and thickness of the die increases the radiation heat transfer from all device surfaces. Additionally, Fig. 13 shows the radiant heat flux from the die surfaces of the device. The radiant heat flux is 10.356 kW in the base case and becomes zero in the insulation case (where heat transfer is negligible). For cases 3 to 8, these values are 4.48, 6.3, 8.25, 9.28, and 10.08 kW, respectively. The die surfaces account for approximately 50% of the heat losses from all device surfaces. Insulating the die surface nearly eliminates the heat loss from the surface. At a constant die height, radiation heat loss increases with a larger die thickness.

5. Correlation analysis of thermal losses and electrical power

A correlation analysis between heat losses and electrical power is useful for achieving optimal conditions. Since the amount of heat loss is directly related to the electrical power, minimizing thermal losses will reduce the input electrical power. The larger thickness of the die results in an increase in the pass cross-sectional area for electric current. As a result, the Joule heating mechanism generates more heat. This leads to an increase in the die temperature and the radiation heat transfer rate, as illustrated in Fig. 4. This leads to a rise in total radiant heat losses. To compensate for heat losses and reach the desired temperature of 2000 °C, more electrical power is required as thermal losses rise (see Fig. 10). At constant thickness, the magnitude of radiation heat losses rises with an increase in die height. This is attributed to the simultaneous increase in radiation surface and the passing cross-sectional area of the electric current, increasing the die surface temperature (see Fig. 5). Therefore, an increase in die height requires higher input electrical power (see Fig. 10). Based on numerical simulation, it is determined that the utilization of insulation in the entire surface of the device necessitates a voltage of 1.66 V and a current of 1980 A. Consequently, this results in a reduction of the required input electrical power to 3.28 kW.

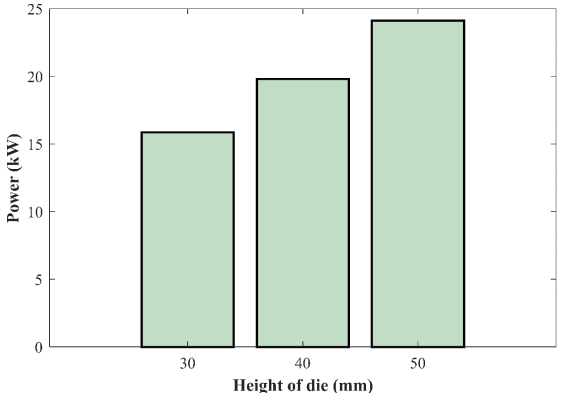

Fig. 11. Power consumption in the various heights of the die (constant thickness of die; t = 17 mm).

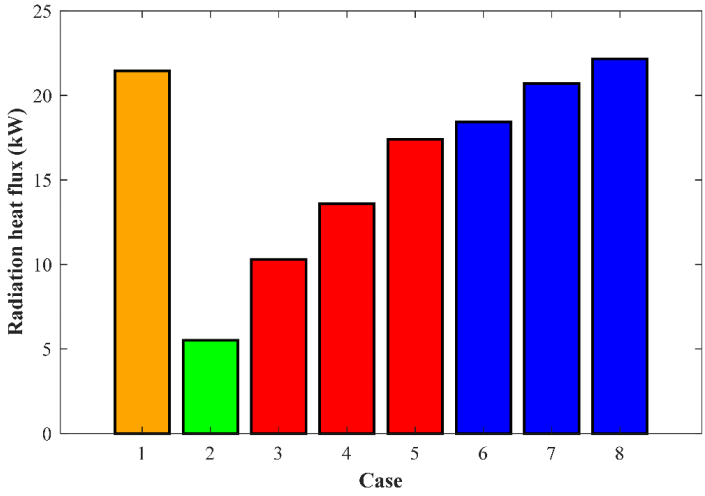

Fig. 12. Radiative heat flux from all surfaces of the SPS device in different cases.

6. Conclusions

A key factor that affects the mechanical properties and microstructure of the sintered samples is the temperature distribution during the sintering process. The main source of heat generation in the SPS process is Joule heating. The electric current density and energy conservation equations were numerically solved using the finite element method in order to determine the temperature and electric current distribution. In the present work, the temperature and electric current distribution during the TiC sample sintering process were simulated numerically using COMSOL Multiphysics software, and the SPS process for TiC samples was optimised by investigating the effect of die geometry (height and thickness) and insulation application. The results showed that the input power consumption was significantly reduced by 63% when compared to the non-insulated case, highlighting the usefulness of insulation in enhancing the SPS process's energy efficiency. Consequently, the effects of the height and thickness of the die were investigated in order to optimise the SPS process. As a result, temperature uniformity is more sensitive to variations in die height than to variations in die thickness. The correlation study between current lines and temperature distribution revealed useful insights into the relationship between electric current and temperature distribution. The results indicated that an increase in die thickness resulted in an increase in the electric current's cross-sectional area, which in effect changed the quantity of electricity required to attain the sintering temperature of 2000 °C.

CRediT authorship contribution statement

Milad Sakkaki: Project administration, Supervision, Validation, Visualization, Methodology, Software, Formal analysis, Investigation, Writing - Review & Editing, Resources.

Milad Foroutani: Visualization, Investigation, Writing-original draft, Software, Data Curation, Resources, Validation.

Peyman Zare: Validation, Writing - Review & Editing, Supervision, Software, Formal analysis, Resources.

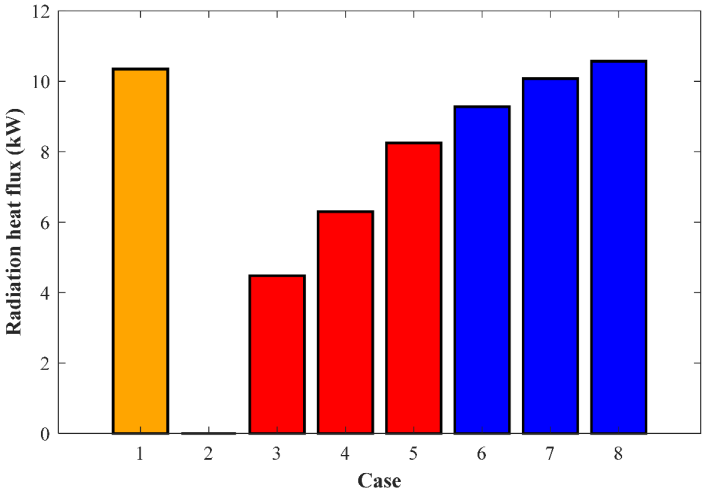

Fig. 13. Radiative heat flux from die surfaces of the SPS device in different cases.

Data availability

The data used in this paper will be accessible upon request.

Declaration of competing interest

The authors declare that they have no known competing financial interests or personal relationships that could have appeared to influence the work reported in this paper. The authors hereby confirm that there is no conflict of interest to disclose.

Funding and acknowledgment

This research received no external funding. The authors have no acknowledgments to declare.

Declaration of Ai and Ai-assisted technologies in the writing process

During the preparation of this work, the authors used AI and AI-assisted technologies to improve the readability and language of the work. After using these tools, the authors reviewed and edited the content as needed and took full responsibility for the publication's content.

References

[1] A.A. Saad, C. Martinez, R.W. Trice, Radiation heat transfer during hypersonic flight: A review of emissivity measurement and enhancement approaches of ultra-high temperature ceramics, Int. J. Ceram. Eng. Sci. 5 (2023) e10171. https://doi.org/10.1002/ces2.10171.

[2] E. Wuchina, E. Opila, M. Opeka, W. Fahrenholtz, I. Talmy, UHTCs: Ultra-High Temperature Ceramic materials for extreme environment applications, Electrochem. Soc. Interface. 16 (2007) 30–36. https://doi.org/10.1149/2.F04074IF/XML.

[3] S.R. Levine, E.J. Opila, M.C. Halbig, J.D. Kiser, M. Singh, J.A. Salem, Evaluation of ultra-high temperature ceramics foraeropropulsion use, J. Eur. Ceram. Soc. 22 (2002) 2757–2767. https://doi.org/10.1016/S0955-2219(02)00140-1.

[4] M.J. Gasch, D.T. Ellerby, S.M. Johnson, Ultra High Temperature Ceramic Composites, Handbook of Ceramic Composites, Springer, Boston, MA. (2005) 197–224. https://doi.org/10.1007/0-387-23986-3_9.

[5] B. Liu, Y. Wang, C. Li, Z. Tian, L. Cheng, Research on the thermal shock simulation of the super high speed aircraft, Mech. Adv. Mater. Struct. 30 (2023) 1889–1896. https://doi.org/10.1080/15376494.2022.2046218.

[6] B.C. Wyatt, S.K. Nemani, G.E. Hilmas, E.J. Opila, B. Anasori, Ultra-high temperature ceramics for extreme environments, Nat. Rev. Mater. 2023 (2023) 1–17. https://doi.org/10.1038/s41578-023-00619-0.

[7] A. Nisar, R. Hassan, A. Agarwal, K. Balani, Ultra-high temperature ceramics: Aspiration to overcome challenges in thermal protection systems, Ceram. Int. 48 (2022) 8852–8881. https://doi.org/10.1016/J.CERAMINT.2021.12.199.

[8] A. Lynam, A.R. Romero, F. Xu, R.W. Wellman, T. Hussain, Thermal Spraying of Ultra-High Temperature Ceramics: A Review on Processing Routes and Performance, J. Therm. Spray Technol. 31 (2022) 745–779. https://doi.org/10.1007/s11666-022-01381-5.

[9] S. Kumar, A. Singh, Development, and characterisation of ultra-high-temperature ceramics composite (UHTC), Adv. Mater. Process. Technol. (2022) 1–10. https://doi.org/10.1080/2374068X.2022.2117443.

[10] F. Valizadeh Harzand, S. Anzani, A. Babapoor, Recent advances in synthesis of ultra-high temperature ceramic matrix composites, Synth. Sinter. 2 (2022) 186–190. https://doi.org/10.53063/synsint.2022.2475.

[11] V.K.V. Pasagada, N. Yang, C. Xu, Electron beam sintering (EBS) process for Ultra-High Temperature Ceramics (UHTCs) and the comparison with traditional UHTC sintering and metal Electron Beam Melting (EBM) processes, Ceram. Int. 48 (2022) 10174–10186. https://doi.org/10.1016/j.ceramint.2021.12.229.

[12] M. Jaberi Zamharir, M. Zakeri, M. Razavi, Challenges toward applying UHTC-based composite coating on graphite substrate by spark plasma sintering, Synth. Sinter. 1 (2021) 202–210. https://doi.org/10.53063/synsint.2021.1452.

[13] D. Ni, Y. Cheng, J. Zhang, J.-X. Liu, J. Zou, et al., Advances in ultra-high temperature ceramics, composites, and coatings, J. Adv. Ceram. 11 (2022) 1–56. https://doi.org/10.1007/s40145-021-0550-6.

[14] J. Binner, M. Porter, B. Baker, J. Zou, V. Venkatachalam, et al., Selection, processing, properties and applications of ultra-high temperature ceramic matrix composites, UHTCMCs – a review, Int. Mater. Rev. 65 (2020) 389–444. https://doi.org/10.1080/09506608.2019.1652006.

[15] E. Ghasali, M. Shahedi Asl, Microstructural development during spark plasma sintering of ZrB2–SiC–Ti composite, Ceram. Int. 44 (2018) 18078–18083. https://doi.org/10.1016/J.CERAMINT.2018.07.011.

[16] M.S. Asl, B. Nayebi, Z. Ahmadi, M.J. Zamharir, M. Shokouhimehr, Effects of carbon additives on the properties of ZrB2–based composites: A review, Ceram. Int. 44 (2018) 7334–7348. https://doi.org/10.1016/J.CERAMINT.2018.01.214.

[17] K. Maca, Microstructure evolution during pressureless sintering of bulk oxide ceramics, Process. Appl. Ceram. 3 (2009) 13–17. https://doi.org/10.2298/PAC0902013M.

[18] Z. Zhang, X. Duan, B. Qiu, L. Chen, P. Zhang, et al., Microstructure evolution and grain growth mechanisms of h-BN ceramics during hot-pressing, J. Eur. Ceram. Soc. 40 (2020) 2268–2278. https://doi.org/10.1016/J.JEURCERAMSOC.2020.02.011.

[19] M.H. Lee, J.H. Park, S.D. Park, J.S. Rhyee, M.W. Oh, Grain growth mechanism and thermoelectric properties of hot press and spark plasma sintered Na-doped PbTe, J. Alloys Compd. 786 (2019) 515–522. https://doi.org/10.1016/J.JALLCOM.2019.01.387.

[20] Z.A. Munir, U. Anselmi-Tamburini, M. Ohyanagi, The effect of electric field and pressure on the synthesis and consolidation of materials: A review of the spark plasma sintering method, J. Mater. Sci. 41 (2006) 763–777. https://doi.org/10.1007/s10853-006-6555-2.

[21] J. Guignard, M. Prakasam, A. Largeteau, High Pressure (HP) in Spark Plasma Sintering (SPS) Processes: Application to the Polycrystalline Diamond, Materials. 15 (2022) 4804. https://doi.org/10.3390/ma15144804.

[22] Y. Liu, S. Ge, Y. Huang, Z. Huang, D. Zhang, Influence of Sintering Process Conditions on Microstructural and Mechanical Properties of Boron Carbide Ceramics Synthesized by Spark Plasma Sintering, Materials. 14 (2021) 1100. https://doi.org/10.3390/ma14051100.

[23] V. Mamedov, Spark plasma sintering as advanced PM sintering method, Powder Metall. 45 (2002) 322–328. https://doi.org/10.1179/003258902225007041.

[24] H. Ding, Z. Zhao, J. Jin, L. Deng, P. Gong, X. Wang, Densification mechanism of Zr-based bulk metallic glass prepared by two-step spark plasma sintering, J. Alloys Compd. 850 (2021) 156724. https://doi.org/10.1016/j.jallcom.2020.156724.

[25] M. Tokita, Progress of spark plasma sintering (Sps) method, systems, ceramics applications and industrialization, Ceramics. 4 (2021) 160–198. https://doi.org/10.3390/ceramics4020014.

[26] A. Nisar, C. Zhang, B. Boesl, A. Agarwal, Unconventional materials processing using spark plasma sintering, Ceramics. 4 (2021) 20–39. https://doi.org/10.3390/ceramics4010003.

[27] S. Samal, O. Molnárová, F. Průša, J. Kopeček, L. Heller, et al., Net-shape NiTi shape memory alloy by spark plasma sintering method, Appl. Sci. 11 (2021) 1–18. https://doi.org/10.3390/app11041802.
[28] O. Guillon, J. Gonzalez-Julian, B. Dargatz, T. Kessel, G. Schierning, et al., Field-Assisted Sintering Technology/Spark Plasma Sintering: Mechanisms, Materials, and Technology Developments, Adv. Eng. Mater. 16 (2014) 830–849. https://doi.org/10.1002/adem.201300409.
[29] Y. Pazhouhanfar, S.A. Delbari, M. Shahedi Asl, S. Shaddel, M. Pazhouhanfar, et al., Characterization of spark plasma sintered TiC–Si3N4 ceramics, Int. J. Refract. Met. Hard Mater. 95 (2021) 105444. https://doi.org/10.1016/j.ijrmhm.2020.105444.
[30] M. Saravana Kumar, S. Rashia Begum, M. Vasumathi, C.C. Nguyen, Q. Van Le, Influence of molybdenum content on the microstructure of spark plasma sintered titanium alloys, Synth. Sinter. 1 (2021) 41–47. https://doi.org/10.53063/synsint.2021.1114.
[31] B. Cai, H.-L. Zhuang, J. Pei, B. Su, J.-W. Li, et al., Spark plasma sintered Bi-Sb-Te alloys derived from ingot scrap: Maximizing thermoelectric performance by tailoring their composition and optimizing sintering time, Nano Energy. 85 (2021) 106040. https://doi.org/10.1016/j.nanoen.2021.106040.
[32] M. Sakkaki, S.M. Arab, In-situ synthesized phases during the spark plasma sintering of g-C3N4 added TiB2 ceramics: A thermodynamic approach, Synth. Sinter. 3 (2023) 73–78. https://doi.org/10.53063/SYNSINT.2023.32151.
[33] B. Li, Z. Yang, J. Jia, Y. Zhong, X. Liu, et al., High temperature thermal physical performance of BeO/UO2 composites prepared by spark plasma sintering (SPS), Scr. Mater. 142 (2018) 70–73. https://doi.org/10.1016/j.scriptamat.2017.08.031.
[34] A. Cincotti, A.M. Locci, R. Orrù, G. Cao, Modeling of SPS apparatus: Temperature, current and strain distribution with no powders, AIChE J. 53 (2007) 703–719. https://doi.org/10.1002/aic.11102.
[35] M. Sakkaki, S.M. Arab, Non-catalytic applications of g-C3N4: A brief review, Synth. Sinter. 2 (2022) 176–180. https://doi.org/10.53063/SYNSINT.2022.24126.
[36] S. Zhang, W. Liu, W. Wang, Y. Gao, A. Wang, et al., Numerical Simulation of Physical Fields during Spark Plasma Sintering of Boron Carbide, Materials. 16 (2023) 3967. https://doi.org/10.3390/ma16113967.
[37] M. Nöthe, J. Trapp, A.S. Semenov, B. Kieback, T. Wallmersperger, Miniaturised test-setup for Spark Plasma Sintering – experimental and numerical investigations, Powder Metall. 66 (2023) 461–471. https://doi.org/10.1080/00325899.2023.2219511.
[38] A.S. Semenov, J. Trapp, M. Nöthe, O. Eberhardt, B. Kieback, T. Wallmersperger, Thermo-electro-mechanical modeling of spark plasma sintering processes accounting for grain boundary diffusion and surface diffusion, Comput. Mech. 67 (2021) 1395–1407. https://doi.org/10.1007/s00466-021-01994-7.
[39] E. Ranjbarpour Niari, M. Vajdi, M. Sakkaki, S. Azizi, F. Sadegh Moghanlou, M. Shahedi Asl, Finite element simulation of disk-shaped HfB 2 ceramics during spark plasma sintering process, Int. J. Appl. Ceram. Technol. 19 (2022) 344–357. https://doi.org/10.1111/ijac.13886.
[40] S. Mohammad Bagheri, M. Vajdi, F. Sadegh Moghanlou, M. Sakkaki, M. Mohammadi, et al., Numerical modeling of heat transfer during spark plasma sintering of titanium carbide, Ceram. Int. 46 (2020) 7615–7624. https://doi.org/10.1016/j.ceramint.2019.11.262.
[41] M. Sakkaki, F.S. Moghanlou, M. Vajdi, M.S. Asl, M. Mohammadi, M. Shokouhimehr, Numerical simulation of heat transfer during spark plasma sintering of zirconium diboride, Ceram. Int. 46 (2020) 4998–5007. https://doi.org/10.1016/j.ceramint.2019.10.240.
[42] H. Conrad, A.F. Sprecher, W.D. Cao, X.P. Lu, Electroplasticity—the effect of electricity on the mechanical properties of metals, JOM. 42 (1990) 28–33. https://doi.org/10.1007/BF03221075.
[43] S.R. Mousavi Aghdam, P. Zare, A. Babaei, R. Mohajery, The Superiority of Turbulent Current of Water-based Optimization for Speed Control of Brushless DC Motor, 8th International Conference on Technology and Energy Management (ICTEM). (2023) 1–7. https://doi.org/10.1109/ICTEM56862.2023.10084323.
[44] P. Zare, A. Dejamkhooy, I.F. Davoudkhani, Efficient expansion planning of modern multi-energy distribution networks with electric vehicle charging stations: A stochastic MILP model, Sustain. Energy Grids Netw. 38 (2024) 101225. https://doi.org/10.1016/J.SEGAN.2023.101225.
[45] P. Zare, I.F. Davoudkhani, R. Mohajeri, R. Zare, H. Ghadimi, Performance Analysis and Design of FOPDF(1+FOPI) Robust Controller Using Slim Mould Algorithm for Frequency Control in Offshore Fixed Platform Microgrid, 12th Smart Grid Conference (SGC). (2022) 1–7. https://doi.org/10.1109/SGC58052.2022.9998979.
[46] R. Mohajery, H. Shayeghi, P. Zare, Optimal FOTID Controller Design for Regulation of DC Motor Speed, Int. J. Tech. Phys. Probl. Eng. 14 (2022) 57–63.
[47] Y. Achenani, M. Saâdaoui, A. Cheddadi, G. Bonnefont, G. Fantozzi, Finite element modeling of spark plasma sintering: Application to the reduction of temperature inhomogeneities, case of alumina, Mater Des. 116 (2017) 504–514. https://doi.org/10.1016/j.matdes.2016.12.054.
[48] K. Vanmeensel, A. Laptev, J. Hennicke, J. Vleugels, O. Van der Biest, Modelling of the temperature distribution during field assisted sintering, Acta Mater. 53 (2005) 4379–4388. https://doi.org/10.1016/j.actamat.2005.05.042.
[49] C. Manière, A. Pavia, L. Durand, G. Chevallier, K. Afanga, C. Estournès, Finite-element modeling of the electro-thermal contacts in the spark plasma sintering process, J. Eur. Ceram. Soc. 36 (2016) 741–748. https://doi.org/10.1016/j.jeurceramsoc.2015.10.033.
[50] T. Matsumoto, A. Ono, Specific heat capacity and emissivity measurements of ribbon-shaped graphite using pulse current heating, Int. J. Thermophys. 16 (1995) 267–275. https://doi.org/10.1007/BF01438977/METRICS.
[51] T. Voisin, L. Durand, N. Karnatak, S. Le Gallet, M. Thomas, et al., Temperature control during Spark Plasma Sintering and application to up-scaling and complex shaping, J. Mater. Process. Technol. 213 (2013) 269–278. https://doi.org/10.1016/J.JMATPROTEC.2012.09.023.
[52] C. Manière, A. Pavia, L. Durand, G. Chevallier, V. Bley, et al., Pulse analysis and electric contact measurements in spark plasma sintering, Electric Power Syst. Res. 127 (2015) 307–313. https://doi.org/10.1016/j.epsr.2015.06.009.
[53] A. Pavia, L. Durand, F. Ajustron, V. Bley, G. Chevallier, et al., Electro-thermal measurements and finite element method simulations of a spark plasma sintering device, J. Mater. Process. Technol. 213 (2013) 1327–1336. https://doi.org/10.1016/j.jmatprotec.2013.02.003.
[54] F.S. Moghanlou, M. Vajdi, M. Sakkaki, S. Azizi, Effect of graphite die geometry on energy consumption during spark plasma sintering of zirconium diboride, Synth. Sinter. 1 (2021) 54–61. https://doi.org/10.53063/synsint.2021.117.
[55] M. Sakkaki, M. Naderi, M. Vajdi, F.S. Moghanlou, A.T. Beris, A simulative approach to obtain higher temperatures during spark plasma sintering of ZrB2 ceramics by geometry optimization, Synth. Sinter. 3 (2023) 248–258. https://doi.org/10.53063/SYNSINT.2023.34178.
[56] M. Le Flem, A. Allemand, S. Urvoy, D. Cédat, C. Rey, Microstructure and thermal conductivity of Mo–TiC cermets processed by hot isostatic pressing, J. Nucl. Mater. 380 (2008) 85–92. https://doi.org/10.1016/j.jnucmat.2008.01.033.
[57] N. Durlu, Titanium carbide based composites for high temperature applications, J. Eur. Ceram. Soc. 19 (1999) 2415–2419. https://doi.org/10.1016/S0955-2219(99)00101-6.
[58] W.S. Williams, The thermal conductivity of metallic ceramics, JOM. 50 (1998) 62–66. https://doi.org/10.1007/s11837-998-0131-y.